

Showcasing research from the Group of Prof. Wensheng Bian at the Institute of Chemistry, Chinese Academy of Sciences, China

A diabatization method based upon integrating the diabatic potential gradient difference

Nonadiabatic processes involving conical intersections are very important in many fields. Here, we propose a diabatization method which is based on integrating the diabatic potential gradient difference. The method is capable of performing high-precision adiabatic-to-diabatic transformations, with a unique advantage in effectively handling the significant fluctuations in derivative-couplings caused by conical intersection seams. It is expected to be extended to study systems involving many electronic states, and would become a useful tool for dynamics simulations of nonadiabatic processes.

As featured in:



See Haitao Ma, Wensheng Bian et al., *Phys. Chem. Chem. Phys.*, 2024, **26**, 16477.



Cite this: *Phys. Chem. Chem. Phys.*,
2024, 26, 16477

A diabatization method based upon integrating the diabatic potential gradient difference[†]

Fengyi Li,^{ab} Xiaoxi Liu,^{ab} Haitao Ma^{ID *a} and Wensheng Bian^{ID *ab}

In this work we develop a new scheme to construct a diabatic potential energy matrix (DPEM). We propose a diabatization method which is based on integrating the diabatic potential gradient difference to diabatize adiabatic *ab initio* energies. This method is capable of performing high-precision adiabatic-to-diabatic transformations, with a unique advantage in effectively handling the significant fluctuations in derivative-couplings caused by conical intersection (CI) seams. The above scheme is applied to the DPEM construction of the $\text{Na}(3p) + \text{H}_2 \rightarrow \text{NaH} + \text{H}$ reaction. The fitting data including adiabatic energies, energy gradients and derivative-couplings obtained from a previous benchmark DPEM are diabatized and fitted using a general neural network fitting procedure to generate the DPEM. The produced DPEM can effectively describe nonadiabatic processes involving different electronic states. We further perform quantum dynamical calculations on the new DPEM and the previous benchmark DPEM, and the obtained results demonstrate the effectiveness of our scheme.

Received 26th January 2024,
Accepted 10th April 2024

DOI: 10.1039/d4cp00375f

rsc.li/pccp

1 Introduction

Within the Born–Oppenheimer (BO) approximation, various electronic structure methods are employed to solve the electronic Schrödinger equation. This process yields adiabatic potential energy surfaces (APESs) which are commonly used in reaction dynamics studies. However, the BO approximation may not be adequate for chemical reactions that involve nonadiabatic processes, which are known to be very important in many fields such as DNA photodamage, photocatalysis and astrochemistry.^{1–5} Therefore, the reaction dynamics studies of nonadiabatic processes involving potential energy surface intersections have attracted great research interest.^{6–9} In theoretical studies, the nonadiabatic reaction dynamics calculations can be carried out in either the adiabatic or diabatic representation. However, the DPEM construction remains a challenge nowadays.

Due to the non-uniqueness of the diabatic representation, there are various methods of diabatization.^{10–25} According to the type of information used, these methods of diabatization can be grouped into a few categories: ansatz, property-based and derivative-coupling-based diabatization.^{21,22,26} The adiabatic electronic structure data are reproduced very well by fitting a predetermined physical model in the ansatz method,

which is a widely used diabatization scheme using the block-diagonalization algorithm.^{19,22} One of the great advantages of the ansatz method is that it expands the adiabatic wave functions into only a low order of Taylor expansion in the normal coordinates around a reference geometry. The property-based diabatization is appealing due to its simplicity and widely used since almost every Hermitian operator can be used to generate a diabatic representation, such as orbitals, projection of dipoles, the entire dipole matrix, quadrupoles and angular momenta.^{13,22} Based on orbital transformations, the threefold- and fourfold-way direct diabatization schemes were popular for yielding diabatic molecular orbitals. The third type of diabatization uses the derivative-coupling information and it is in principle the most accurate method,^{27,28} as the derivative-couplings are directly used to diabatize the electronic states. The shortcoming of the derivative-coupling method is that it is only implemented in a limited number of quantum chemistry programs, which limits its application to larger systems. However, this kind of method has been quite successfully applied to a series of reactive systems.^{29–33} The fitting of derivative-couplings *via* least-squares minimizes the residual-couplings, providing a reliable diabatic energy matrix representation for simulating nonadiabatic processes, which was first introduced in the Zhu–Yarkony diabatization strategy.²⁶ The rigorous diabatic representation does not exist for polyatomic (including triatomic) molecules due to the fact that the rigorous diabatic electronic wave functions could not be obtained with limited calculations and methods,^{6,7,34–36} hence it is referred to as quasi-diabatic in the rest of this work. Very recently, Truhlar and co-workers achieved DPEM smoothness by combining the deep

^a Beijing National Laboratory for Molecular Sciences, Institute of Chemistry, Chinese Academy of Sciences, Beijing 100190, China. E-mail: mht@iccas.ac.cn, bian@iccas.ac.cn

^b University of Chinese Academy of Sciences, Beijing, 100049, China

[†] Electronic supplementary information (ESI) available. See DOI: <https://doi.org/10.1039/d4cp00375f>

neural network architecture with diabatization procedures.^{5,22} Achieving accurate diabatization through machine learning frequently necessitates a significant volume of data, while the *ab initio* computations involved in processing this data can be time-consuming.

In this work, we propose a hybrid scheme that combines a diabatization approach based on the diabatic potential gradient difference with the neural network (NN) technique for the construction of DPEMs. The *ab initio* derived DPEMs are of paramount importance in quantum dynamics, particularly for an accurate description of non-adiabatic processes, which has long been a primary objective in the field. We apply our scheme to the development of DPEMs for the two lowest electronic states of NaH₂ to illustrate the accuracy and effectiveness of our new diabatization method. The Na(3p) + H₂ → NaH + H reaction serves as a prototype for the study of the collisional quenching of electronically excited alkali and alkaline earth atoms.^{10,37–41} This reaction is also representative of a fundamental class of nonadiabatic processes occurring through an excited-state potential energy well that intersects with the ground electronic state conically, and such processes are of particular interest in both experimental and theoretical studies.^{42,43} In this work, we construct an analytical 2 × 2 DPEM for the two lowest-lying 1,2²A' states of the title system using our scheme, which generates coupled quasi-diabatic potentials over a wide range of geometries. The organization of the present article is as follows. Section 2 introduces our theoretical approach for constructing a DPEM. The properties of the DPEM and further time-dependent wave packet calculations are presented and discussed in detail in Section 3. Finally, a brief summary is given in Section 4.

2 Theoretical approach

Derivative-coupling-based methods are in principle the most accurate ones for constructing quasi-diabatic states.^{14,44,45} In most derivative-coupling-based diabatization,^{46–49} the interstate couplings are obtained by

$$\vec{h} = \vec{\tau}_{1,2}(E_2^a - E_1^a) \quad (1)$$

where E_2^a and E_1^a are the energies for 2, 1 adiabatic states in the two-state model. $\vec{\tau}_{1,2}$ is the derivative-coupling vector between the two adiabatic states, which is a vector with $3 \times N$ elements, where N is the number of atoms. In the two-state coupling model, the nonadiabatic coupling matrix τ has a very simple form:

$$\tau = \begin{pmatrix} 0 & \vec{\tau}_{1,2} \\ -\vec{\tau}_{1,2} & 0 \end{pmatrix}. \quad (2)$$

The corresponding adiabatic-to-diabatic transformation (ADT) matrix \mathbf{A} for the two-state model is a real orthogonal matrix of dimension 2 × 2, and it can be presented in the form:

$$\mathbf{A} = \begin{pmatrix} \cos \lambda & \sin \lambda \\ -\sin \lambda & \cos \lambda \end{pmatrix} \quad (3)$$

where λ is called the mixing angle. Here, λ can be obtained by solving the equation:

$$\nabla \lambda + \vec{\tau}_{1,2} = 0 \quad (4)$$

Ignoring the sign of $\vec{\tau}_{1,2}$, we get the key equation in ADT:

$$\nabla \lambda = \vec{\tau}_{1,2} \quad (5)$$

The ADT equation is:

$$\mathbf{E}^d = \mathbf{A}^T \mathbf{E}^a \mathbf{A} \quad (6)$$

which could be expanded as

$$E_{1,1}^d = E_1^a \cos^2 \lambda + E_2^a \sin^2 \lambda \quad (7)$$

$$E_{2,2}^d = E_2^a \cos^2 \lambda + E_1^a \sin^2 \lambda \quad (8)$$

$$E_{1,2}^d = (E_1^a - E_2^a) \sin \lambda \cos \lambda \quad (9)$$

where E_2^a and E_1^a are the energies for the adiabatic states, $E_{1,1}^d$ and $E_{2,2}^d$ are the energies for the diabatic states, and $E_{1,2}^d$ is the coupling surface.

As shown in eqn (5), simply integrating $\vec{\tau}_{1,2}$ in all directions could be one of the most direct ways to obtain the mixing angle, and then the diabatic energies are transformed from the adiabatic energies *via* the ADT matrix. However, the fluctuations of the values of $\vec{\tau}_{1,2}$ would lead to the inaccuracy of the result of numerical integration, especially when a point in the grid incidentally has an extremely large value of $\vec{\tau}_{1,2}$. An alternative is to fit $\vec{\tau}_{1,2}$ with an appropriate function so that the result of the indefinite integral of this function could be used as the mixing angle. The numerical integration in a shorter step length for the functions that could not give an indefinite integral would also lead to a much more accurate result than integrating $\vec{\tau}_{1,2}$ directly. However, it is very difficult to find such a function to fit $\vec{\tau}_{1,2}$ because of the fluctuations of the values. In our test using a feedforward neural network^{50,51} with 3 hidden layers and 3 × 20 hidden neurons, the least root-mean-square error (RMSE) fitting error of $\vec{\tau}_{1,2}$ is about 0.1 bohr⁻¹.

In some derivative-coupling-based diabatization methods,^{6,7,31,32} the interstate couplings were fitted instead. Due to the approximate negative correlation between $(E_2^a - E_1^a)$ and $\vec{\tau}_{1,2}$, the interstate coupling becomes a much smoother function than the derivative-coupling; however, the existence of protrusions caused by singularities still hinders the fitting. So it is not recommended to fit the derivative or interstate couplings directly, because of the divergence problem in the conical intersection regions. Recently, a smart approach²⁵ was proposed in which a so-called modified derivative-coupling term, rather than the derivative or interstate coupling, is incorporated in the quasi-diabatic Hamiltonian. This modified term behaves similarly to the original derivative-coupling in regions where the two states have different energies, but effectively avoids singularities when degeneracy occurs, thereby preserving the essential characteristics of the derivative-coupling.

2.1 Diabatization by integrating the diabatic potential gradient difference

Integrating the derivative couplings or interstate couplings would introduce the risk of imprecision in determining the

mixing angle and, consequently, the electronic state energies. Here, we propose to use a new integrand in our diabatization method, defined as $\nabla(E_{1,1}^d - E_{2,2}^d)$, representing the diabatic potential gradient difference, and it could be obtained in the following way. Eqn (7) directly subtracting by eqn (8) results in

$$\begin{aligned} E_{1,1}^d - E_{2,2}^d &= (E_1^a - E_2^a) \cos^2 \lambda + (E_2^a - E_1^a) \sin^2 \lambda \\ &= (E_1^a - E_2^a)(\cos^2 \lambda - \sin^2 \lambda) \\ &= (E_1^a - E_2^a) \cos 2\lambda \end{aligned} \quad (10)$$

or

$$\cos 2\lambda = \frac{(E_{1,1}^d - E_{2,2}^d)}{(E_1^a - E_2^a)}. \quad (11)$$

Now we differentiate both sides of eqn (10):

$$\begin{aligned} \nabla(E_{1,1}^d - E_{2,2}^d) &= \nabla((E_1^a - E_2^a) \cos 2\lambda) \\ &= (\nabla(E_1^a - E_2^a)) \cos 2\lambda + (E_1^a - E_2^a)(\nabla \cos 2\lambda) \\ &= (\nabla(E_1^a - E_2^a)) \cos 2\lambda \\ &\quad + (E_1^a - E_2^a)(-\sin 2\lambda) \cdot 2\nabla\lambda \end{aligned} \quad (12)$$

Substituting $\vec{\tau}_{1,2} = \nabla\lambda$ into eqn (12), we obtain

$$\nabla(E_{1,1}^d - E_{2,2}^d) = (\nabla E_1^a - \nabla E_2^a) \cos 2\lambda - 2\vec{\tau}_{1,2}(E_1^a - E_2^a) \sin 2\lambda \quad (13)$$

To simplify eqn (13), we can use vector \vec{h} provided by eqn (1) and \vec{g} defined as the gradient difference in the following form,

$$\vec{g} = \frac{1}{2}(\nabla E_2^a - \nabla E_1^a). \quad (14)$$

Then we have

$$\nabla(E_{1,1}^d - E_{2,2}^d) = -2\vec{g} \cdot \cos 2\lambda + 2\vec{h} \cdot \sin 2\lambda \quad (15)$$

where, $\sin 2\lambda$ can be replaced by $\sqrt{1 - \cos^2 2\lambda}$ in the $\lambda \in [0, \frac{\pi}{2}]$ region,

$$\nabla(E_{1,1}^d - E_{2,2}^d) = -2\vec{g} \cdot \cos 2\lambda + 2\vec{h}\sqrt{1 - \cos^2 2\lambda} \quad (16)$$

Substituting eqn (11) into eqn (16), we obtain

$$\begin{aligned} \nabla(E_{1,1}^d - E_{2,2}^d) &= -2\vec{g} \cdot \frac{(E_{1,1}^d - E_{2,2}^d)}{(E_1^a - E_2^a)} \\ &\quad + 2\vec{h}\sqrt{1 - \left(\frac{(E_{1,1}^d - E_{2,2}^d)}{(E_1^a - E_2^a)}\right)^2} \end{aligned} \quad (17)$$

Vectors \vec{g} and \vec{h} could be obtained using an *ab initio* package, such as Columbus. It is essential to use the original vectors rather than the orthogonalized ones. That is because only the original ones are the direct reflection of the adiabatic gradient difference and the derivative couplings, the orthogonalized ones cannot be defined using eqn (1) and (14). An alternative is to calculate them using E^a , ∇E^a and $\vec{\tau}_{1,2}$ which are obtained during *ab initio* simulations.

Now the diabatic energy difference $(E_{1,1}^d - E_{2,2}^d)$ could be calculated by solving eqn (17). To provide the diabatic energy of

the two states, respectively, the sum of diabatic energy $(E_{1,1}^d + E_{2,2}^d)$ is needed, so we add eqn (7) and (8) and get

$$\begin{aligned} (E_{1,1}^d + E_{2,2}^d) &= (E_1^a + E_2^a) \cos^2 \lambda + (E_2^a + E_1^a) \sin^2 \lambda \\ &= (E_1^a + E_2^a)(\cos^2 \lambda + \sin^2 \lambda) \\ &= (E_1^a + E_2^a) \end{aligned} \quad (18)$$

The diabatic energy can now be obtained using

$$\begin{aligned} E_{1,1}^d &= \frac{1}{2}((E_{1,1}^d + E_{2,2}^d) + (E_{1,1}^d - E_{2,2}^d)) \\ &= \frac{1}{2}((E_1^a + E_2^a) + (E_{1,1}^d - E_{2,2}^d)) \end{aligned} \quad (19)$$

and

$$\begin{aligned} E_{2,2}^d &= \frac{1}{2}((E_{1,1}^d + E_{2,2}^d) - (E_{1,1}^d - E_{2,2}^d)) \\ &= \frac{1}{2}((E_1^a + E_2^a) - (E_{1,1}^d - E_{2,2}^d)). \end{aligned} \quad (20)$$

The diabatic coupling term between the two states is also needed in non-adiabatic dynamics, which is provided below:

$$\begin{aligned} E_{1,2}^d &= (E_1^a - E_2^a) \sin \lambda \cos \lambda \\ &= \frac{1}{2}(E_1^a - E_2^a) \sin 2\lambda \end{aligned} \quad (21)$$

To avoid using the mixing angle λ , we again replace $\sin 2\lambda$ with $\sqrt{1 - \left(\frac{(E_{1,1}^d - E_{2,2}^d)}{(E_1^a - E_2^a)}\right)^2}$ and get

$$\begin{aligned} E_{1,2}^d &= \frac{1}{2}(E_1^a - E_2^a) \sqrt{1 - \left(\frac{(E_{1,1}^d - E_{2,2}^d)}{(E_1^a - E_2^a)}\right)^2} \\ &= \frac{1}{2}\sqrt{(E_1^a - E_2^a)^2 - (E_{1,1}^d - E_{2,2}^d)^2} \end{aligned} \quad (22)$$

Combining $E_{1,1}^d$, $E_{2,2}^d$ and $E_{1,2}^d$, we get the final DPEM \mathbf{E}^d , with the form:

$$\mathbf{E}^d = \begin{pmatrix} E_{1,1}^d & E_{1,2}^d \\ E_{1,2}^d & E_{2,2}^d \end{pmatrix} \quad (23)$$

In our ADT method, the integration of $\nabla(E_{1,1}^d - E_{2,2}^d)$, which solely relies on the derivative-couplings, offers a foundation for constructing DPEMs. This construction is achieved without encountering singularities and without resorting to any approximation.

This method can be extended to study systems involving multiple electronic states, since the diabatization of each pair of states could be done using the same method as described above. Here we take a 3-state coupling system as an example, for which the ADT matrix can be written as a product of three 2-in-3-state ADT matrices,³⁴ made up of the functions of 3 mixing angles $\lambda_{1,2}$, $\lambda_{1,3}$ and $\lambda_{2,3}$. Although the mixing angle is avoided to be used directly in the scheme described

above, it can still be obtained easily after diabatization using the following formula:

$$\lambda = \frac{1}{2} \tan^{-1} \left(\frac{2E_{1,2}^d}{E_{1,1}^d - E_{2,2}^d} \right) \quad (24)$$

Then the diabatic energy matrix could be calculated *via* eqn (6) using the obtained 3-state ADT matrix. To demonstrate the diabatization process, we conducted tests on a simple model system which involves multiple electronic states. As can be seen from Fig. S4 (ESI[†]), the obtained diabatic potentials are reasonable and smooth, and the continuity of the diabatic state PES can be ensured. The details are given in the ESI.[†]

2.2 The neural network fitting

In the above diabatization procedure, the residual-couplings were nearly eliminated. Then we used the feedforward NN method to fit the obtained diabatic surfaces. The inverse of three cartesian coordinates of the system was used as the input of the NN. The NN structure we used to fit diabatic potentials $E_{1,1}^d$ and $E_{2,2}^d$ is 3-8-15-10-3, which has 3 hidden layers and 338 parameters. And the NN structure for $E_{1,2}^d$ is 3-8-10-1, which has 2 hidden layers and 133 parameters. The sizes of our NNs are quite small owing to the smoothness of all the DPEM elements, which are enough to give satisfactory results. The transfer functions of the neurons in the input and output layers are linear functions, and those in the hidden layers were chosen to be hyperbolic tangent functions. The functional form of a sampled NN with the structure of 3-8-10-1 can be written as

$$E = b_{1,4} + \sum_{i=1}^{10} \left(w_{i,3} \cdot \tanh \left(b_{i,3} + \sum_{j=1}^8 \left(w_{j,2} \cdot \tanh \left(b_{j,2} + \sum_{k=1}^3 (w_{k,1} \cdot \text{Inp}_k) \right) \right) \right) \right) \quad (25)$$

where $\text{Inp}_k (k = 1, \dots, 3)$ is the input vector, \tanh is the hyperbolic tangent function, $w_{i,j}$ and $b_{i,j}$ are the weights and bias for the i th neuron of the j th layer, respectively, and E is the output energy or coupling. The weights and bias were optimized using the Levenberg–Marquardt (LM) algorithm in each fitting to minimize the error. The “early stopping” method was used to avoid over fitting, with 70% of the data points randomly picked as the training set, 50% of the rest as the validating set, and the others as the testing set. Thus, the fitting procedure was stopped in such conditions:

(a) The mean-square error gradient of each epoch is smaller than 10^{-10} kcal per mol per epoch.

(b) The damping factor μ in the LM algorithm is larger than 10^{10} .

(c) The RMSE of validating set keeps growing for 10 epochs.

The quality of the fitting NN was measured by RMSE, and 6 best NN fits were averaged over to further reduce the fitting error.

3 Method application: the benchmark NaH₂ reaction system

The purpose of this work is to demonstrate the effectiveness of the developed method in constructing a quasi-diabatic representation. Therefore, instead of performing extensive actual *ab initio* calculations, we generate the fitting data from the available benchmark DPEM³⁹ of Hack and Truhlar (HT).

The Jacobi coordinates R (distance of Na from the center of HH mass), r (bond distance of HH) and γ (the angle between R and r) are used as coordinates to generate the fitting data and for the following dynamical calculations. The grid of points is defined by the following values of R , r and γ :

$$R \in [1.00, 2.00, 3.00, 3.20, 3.30, 3.35, 3.40, 3.45, 3.50, 3.55, 3.60, 3.65, 3.70, 3.80, 3.90, 3.95, 4.00, 5.00, 6.00, 7.00, 8.00, 9.00, 10.00, 12.00, 15.0, 30.0] \text{ bohr};$$

$$r \in [1.00, 1.35, 1.40, 1.45, 1.50, 1.60, 1.70, 1.80, 1.90, 2.00, 2.10, 2.20, 2.50, 3.00, 4.00, 5.00, 6.00, 7.00, 10.00, 15.00, 30.0] \text{ bohr};$$

$$\gamma \in [0.00, 0.01, 0.02, 0.03, 0.04, 0.05, 0.07, 0.10, 0.20, 0.30, 0.40, 0.42, 0.45, 0.46, 0.47, 0.48, 0.49, 0.50] \pi;$$

The geometries with energies greater than 13.0 eV are excluded from the surface construction. The additional geometries around extrema including the potential energy well and the lowest minimum energy crossing point (MEX) are also included. A total of 7318 geometries are assembled, which also include 256 points near the MEX. When the geometry closely approaches the MEX, the relative values of derivative-coupling tend to go to infinitely large. In the construction of our DPEM using the new diabatization method, it is unnecessary to incorporate these geometries very near to the MEX, as they may bring numerical challenges. Therefore, the maximum value of derivative-coupling does not exceed 10 000 bohr⁻¹. This grid offers detailed information of the potential energies and the interstate couplings as *ab initio* data to construct surfaces, and provides a good description of dynamically relevant regions and is sufficient to generate a satisfactory DPEM.

3.1 Features of the DPEM

In the construction of potential energy surfaces for the molecules experiencing significant motion, the relevant group in the Schrödinger equation is the complete nuclear permutation and inversion group, as introduced by Longuet–Higgins.⁵² While electronic energies, energy gradients and derivative-couplings are invariant under group operations, the eigenfunctions are only guaranteed to carry irreducible representations of that group.^{18,53} In this work, the fitting coordinates are the functions based on nuclear distances, designed to be invariant under certain pair(s) of C_{2v} permutation operation. The distributions of the fitting errors for the first two-state $1^2A'$ and $2^2A'$ energies, gradients and derivative-couplings between them are shown in Fig. 1 to illustrate the fitting quality, in which most of the energy fitting errors larger than 0.025 eV are localized in the relative energies higher than 10.0 eV and the rest of them are scattered over the CI seam in the energy region (2.0, 5.0) eV. The largest gradients fitting error is 0.0141 eV.

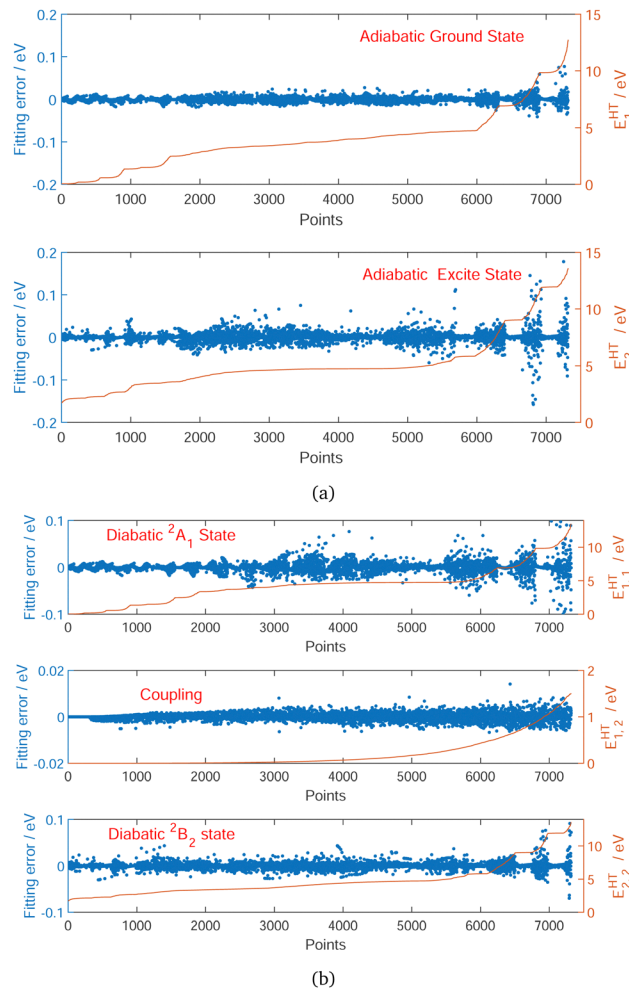


Fig. 1 Fitting error distribution of each point as a function of the relative energy ascending order for adiabatic ground state E_1^{HT} and excited state E_2^{HT} (a), and diabatic ground $E_{1,1}$, couplings $E_{1,2}^{\text{HT}}$ and excited states $E_{2,2}^{\text{HT}}$ (b). Fitting error is defined as the difference between our new DPEM and HT DPEM. Zero of energy in eV is at Na infinitely far from H_2 on the ground surface.

The gradients and their fitting errors for the first 306 points are zero due to the fact that they are determined by C_{2v} symmetry in the processes of diabatization.

A more careful analysis for the fitting of derivative-couplings is provided by Fig. 2 which plots the residual-coupling norm against HT DPEM determined derivative-coupling norm for fitting. The magnitude of the residual-coupling norm, $\|\bar{\tau}_{1,2}^{\text{ours}} - \bar{\tau}_{1,2}^{\text{HT}}\|$, is used to assess the quality of the diabatization so that the quality of diabatization is strictly under control in this work. Despite the fact that a log scale is required to represent a wide range of fitting data, the significant agreement for derivative-coupling fitting in the range of order of 10^{-2} is evident. The small norm of the residual-coupling represents a well quasi-diabatic character of the representation. The residual-coupling cannot disappear completely because the Hamiltonian, \mathbf{H}^d , does not contain the non-removable part of the derivative-coupling. A large absolute percentage fitting error means a large difference between HT DPEM and \mathbf{H}^d determined derivative-

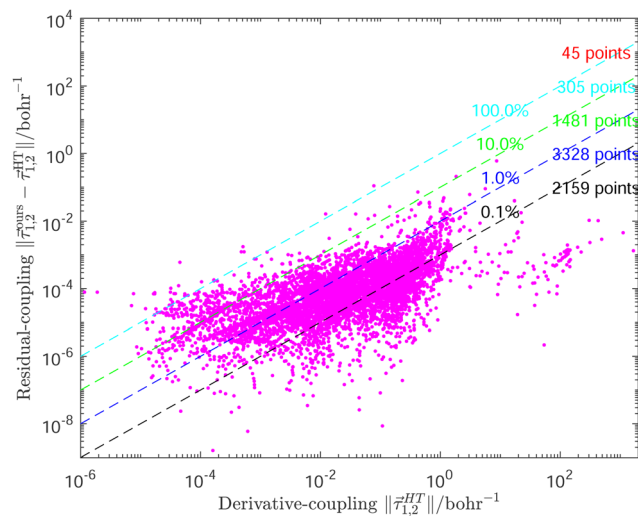


Fig. 2 The magnitudes of the residual-couplings $\|\bar{\tau}_{1,2}^{\text{ours}} - \bar{\tau}_{1,2}^{\text{HT}}\|$ plotted against the magnitude of the derivative-coupling $\|\bar{\tau}_{1,2}^{\text{HT}}\|$. The black, blue, green and cyan lines are the percentage errors of 0.1%, 1.0%, 10.0% and 100.0%, respectively. The number of points with the percentage error lower than 0.1% is 2159, while that larger than 100% is 45.

couplings, however, it does not indicate a significant problem for the small values of derivative-couplings. There are 45 fitting points with the percentage error exceeding 100.0%, which represents around 0.6% of the total points. The geometries of these 45 points are far away from the surface intersection seam in Fig. 3; therefore, the corresponding values of derivative-couplings are small and have insignificant effect on diabatization. Instead, the fitting for these points, close to the surface intersection seam, with large derivative-coupling values is very

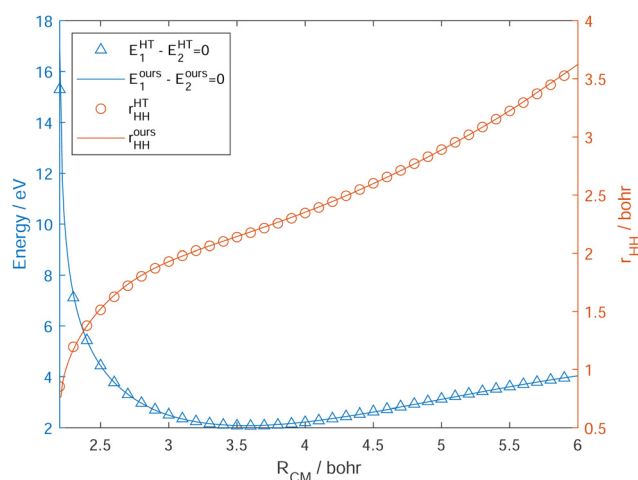


Fig. 3 The intersection seam line (energies from our DPEMs: blue solid line, energies from the HT DPEMs: blue open triangle; our surface geometries: red solid line, HT geometries: red open circles) between the $1^2\text{A}'$ and $2^2\text{A}'$ states of the $\text{Na}(3\text{p}) + \text{H}_2 \rightarrow \text{NaH} + \text{H}$ reaction. The Jacobi coordinates are employed. R_{CM} is the distance of the Na atom to the center of the H_2 mass, r_{HH} is the H_2 bond distance, and the angle γ between vectors R_{CM} and r_{HH} is fixed at $\pi/2$. Zero of energy in eV is at Na infinitely far from H_2 on the ground surface.

good. The number of points with percentage errors ranging from 0.1% to 1.0%, from 1.0% to 10.0% are 2159 and 3328, respectively, which significantly dominates the total points. The fitting errors are quite small compared to the large absolute values for the derivative coupling vector $\vec{\tau}_{1,2}$. It reflects the small difference in the \mathbf{H}^d and HT DPEM determined values for the geometries close to the surface intersection seam in Fig. 3.

The fitting results of the ground state $1^2\text{A}'$ and the excited state $2^2\text{A}'$ are listed in Table 1. The root-mean-square errors (RMSEs) of energies in this fitting are converged to around 0.01 eV, and are found to be 0.0097 eV and 0.0059 eV for $1^2\text{A}'$ and $2^2\text{A}'$ states, respectively, in the energy range under 10.0 eV. It should be noted that 80 percent fitting errors of energies are less than 0.0089 eV and 0.0063 eV, respectively. The RMSEs of the diabatic energies on WYYC DPEM for the Na + H₂ reactive system, constructed using property-based diabatization, are 0.010 eV, 0.020 eV, and 0.009 eV, respectively.⁵⁴ It is noteworthy that the RMSEs for the adiabatic energies in our DPEM constructions are lower than those for the diabatic energies. Moreover, our new DPEM in this work is expected to give an accurate description of the first two states $1^2\text{A}'$ ($^2\text{B}_2$) and $2^2\text{A}'$ ($^2\text{A}_1$) coupled by CI in the quasi-diabatic representation. This reaction starts at the adiabatic $^2\text{B}_2$ surface and then intersects the adiabatic $^2\text{A}_1$ surface to enter into the product channel. The two extrema play an important role in the field of diabatic reaction dynamics, one is an excited-state potential energy well (exciplex) located near $R_{\text{CM}} = 3.92$ bohr and $r_{\text{HH}} = 1.50$ bohr, and the other is the MEX located near $R_{\text{CM}} = 3.59$ bohr and $r_{\text{HH}} = 2.17$ bohr. The properties of the MEX and exciplex from our DPEM and HT DPEM are collected in Table 2. The geometries and the relative energies of the two extrema on our new DPEM agree well with those on the HT DPEM.

Table 2 and Fig. 3 indicate that the results from our new diabatization method based on integrating the diabatic potential gradient difference could reproduce the geometries and energies from the HT DPEM accurately in the intersection seam region. Compared to the property-based diabatization, which is an efficient approach applicable to nearly every Hermitian operator for generating diabatic representations, our new diabatization technique has some advantages in the

Table 1 Root mean square errors (RMSEs) of the NN fitting for the energies, energy gradients, and interstate couplings

Energy ^a	Point range			
	<3.0	[3.0, 5.0]	[5.0, 10.0]	≥10.0
Point number	1845	3983	1217	273
RMSE (E_1) ^b	0.0043	0.0099	0.0141	0.0131
RMSE (E_2) ^b	0.0064	0.0055	0.0063	0.0201
RMSE (∇E_1) ^c	0.0113	0.0242	0.0331	0.0762
RMSE (∇E_2) ^c	0.0085	0.0201	0.0296	0.0842
RMSE (\vec{h}) ^d	0.0025	0.0042	0.0373	0.1966

^a Energies in eV. Zero of energy is at Na infinitely far from H₂ on the ground surface. ^b RMSE for the energies of ground state $1^2\text{A}'$ (E_1) and excited states $2^2\text{A}'$ (E_2) in eV. ^c RMSE for the energy gradients of ground state $1^2\text{A}'$ (∇E_1) and excited states $2^2\text{A}'$ (∇E_2) in eV bohr⁻¹. ^d RMSE for the interstate couplings vector \vec{h} in eV bohr⁻¹.

Table 2 Geometrical parameters and relative energies of extrema including the minimum energy crossing (MEX) point and excited-state potential energy minimum (exciplex). The Jacobi coordinates are employed.^a The bond lengths are in bohr and energies are in eV

		Our	Truhlar's	
		DPEM	HT ^b	DPEM-5G ^c
MEX	Energy ^d	2.064	2.064	1.622
	R_{CM}	3.59	3.59	3.68
	r_{HH}	2.17	2.17	1.98
	γ	$\pi/2$	$\pi/2$	$\pi/2$
Exciplex	Energy ^d	1.700	1.698	1.620
	R_{CM}	3.92	3.93	3.70
	r_{HH}	1.50	1.49	1.93
	γ	$\pi/2$	$\pi/2$	$\pi/2$

^a r_{HH} is the H₂ bond distance in bohr, R_{CM} is the distance of Na from the center of HH mass in bohr, and γ is the angle between R_{CM} and r_{HH} .

^b Ref. 39 NaH₂ surface set 6. ^c Ref. 39,40 NaH₂ surface set 5G. ^d Zero of energy in eV is at Na infinitely far from H₂ on the ground surface.

constructions of the DPEM coupled by CIs. Although the property-based diabatization schemes, using different choices of properties, are appealing in their simplicity, there are subtle difficulties in these methods for diabatization.²² In practice, it is possible that the selected properties confound one another, which makes the diabatization process problematic. Although derived from the same *ab initio* calculations, the geometries of conical intersections (CIs) may exhibit significant variation. For example, at the MEX point on the DK DPEM for the O + H₂ reaction system,¹³ the OH bond distance derived from the configuration coefficients is 3.16 bohr, while it is only 3.04 bohr when determined from the angular momenta. Similarly, the HH bond distance at the MEX, derived from the configuration coefficients, is 2.36 bohr, whereas it is only 2.12 bohr when calculated based on the angular momenta. Moreover, another general problem is that the signs of the diabatic couplings produced by property-based diabatization are not unique.²² These findings underscore the advantages of our new DPEM, which is constructed using the diabatic potential gradient difference method.

The normalized interstate coupling vector and gradient difference vector, and the energies along these vectors are represented in Fig. 4 and Fig. 5, respectively. In terms of atom centered displacements, the interstate coupling vector \vec{h} breaks the C_{2v} symmetry, while the potential gradient difference vector \vec{g} is a symmetry preserving mode. The energy surfaces along the interstate coupling vector \vec{h} and the potential gradient difference vector \vec{g} are, respectively, symmetric and non-symmetric. The energy surface crossing point is a CI point. There are protrusions in the adiabatic energy curves along the interstate coupling vector \vec{h} , which would bring numerical issues in fitting. However, the diabatic energy changes monotonically and smoothly, which makes the fitting much easier. A modified Newton–Raphson method is used in the optimization of CI seam in the present work, to reduce the energy differences to 10^{-4} cm⁻¹ and the geometry errors to less than 10^{-6} bohr.

Fig. 6 shows the fitting accuracy of the constructed \mathbf{H}^d near the seam along the surface conical intersection. Adiabatic

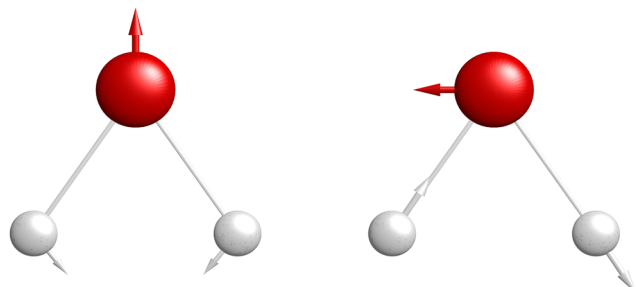


Fig. 4 The normalized potential gradient difference vector \vec{g} (left) and interstate coupling vector \vec{h} (right) at the lowest minimum energy crossing point are indicated pictorially by arrows attached to the atoms. (Red big ball: Na atom and grey small ball: H atom)

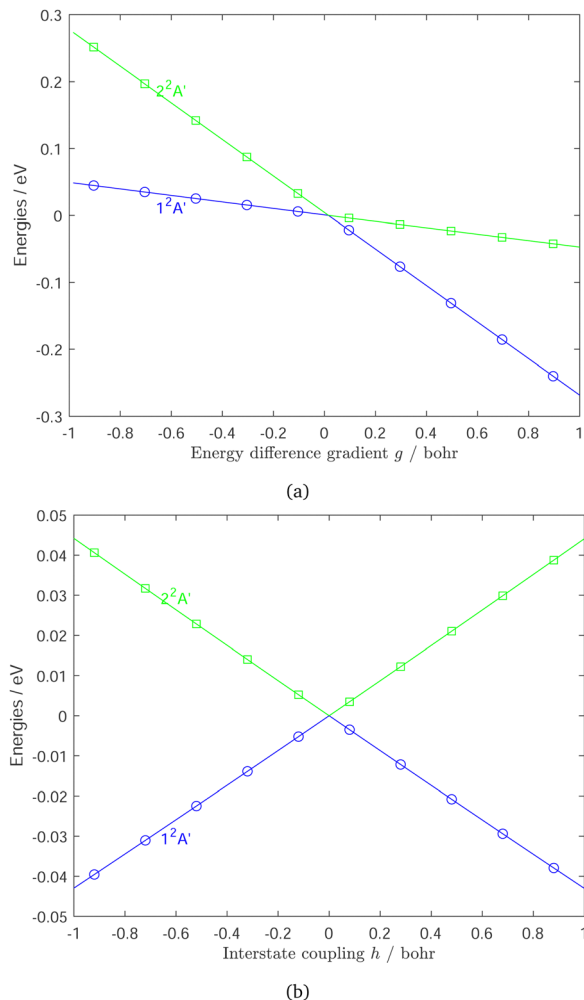


Fig. 5 Potential energy curves along the potential gradient difference \vec{g} direction (a) and the interstate coupling \vec{h} direction (b) at the lowest minimum energy crossing (MEX) point in the g - h plane. Blue line ($1^2A'$) and green line ($2^2A'$) are curves from our DPEM. Blue cycles ($1^2A'$) and green squares ($2^2A'$) are fitting points derived from HT DPEM. Zero of energy in eV is at the MEX.

(E^1 and E^2) and diabatic ($E^{1,1}$ and $E^{2,2}$) potential energy curves with the norm of the derivative-coupling vector ($\|\vec{\tau}_{1,2}\|$) are plotted

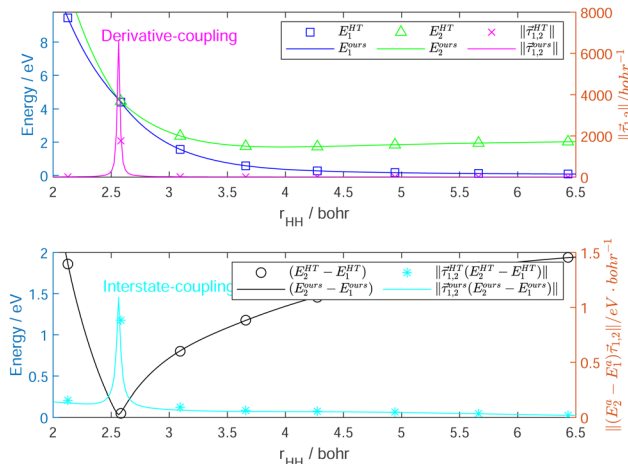


Fig. 6 Adiabatic (E_1 and E_2) potential energy curves with derivative-coupling vector ($\vec{\tau}_{1,2}$) as a function of r_{HH} near the lowest minimum energy crossing point. The corner mark "ours" indicates that the results come from our newly constructed DPEM, rather than HT DPEM. The Jacobi coordinates are employed. r_{HH} is the H_2 bond distance, distance of Na from the center of HH mass R_{CM} is fixed at 4.0 bohr, and the angle γ between R_{CM} and r_{HH} is fixed at $\pi/2$. Zero of energy in eV is at Na infinitely far from H_2 on the ground-state surface.

against r_{HH} near the MEX. The curves are not crossing through the MEX, because otherwise nothing could be seen but an extremely large singularity of the coupling, and no difference between the diabatic and adiabatic energies would appear around the MEX. The errors of the interstate coupling near the MEX region cannot vanish completely because the derivative-couplings are not the real gradients of the mixing angle, and not completely removed by the transformation and the corresponding quasi-diabatic electronic states have a weak dependence on the nuclear coordinates.

The final DPEM and APESs are represented in Fig. 7 and Fig. 8. Fig. 7 shows the first two surfaces of NaH_2 and their conical intersection in both adiabatic and diabatic representation in the g - h plane. The opposite cones could be seen in the adiabatic energy surfaces, while they merge and disappear in the diabatic representation to form two crossing smooth surfaces. Fig. 8 shows the first two surfaces of NaH_2 in adiabatic and diabatic representation in the Jacobi coordinates with the distance of Na from the center of HH mass fixed at 3.0 bohr. In this perspective, the CI seams could be well described in the adiabatic energy surfaces, while it is transformed to an ordinary intersection in the diabatic representation. It is important to note that the energy hyper-surfaces are smoothed in both 3 dimensions of the reactive system in the diabatic representation, which are much easier to fit than the adiabatic energy surfaces.

3.2 Dynamics on the DPEM

In this work, the non-adiabatic coupling effect of the CI between the two states is carefully considered to perform the adiabatic-diabatic transformation by integrating the diabatic potential gradient difference fitting procedure. Accurate

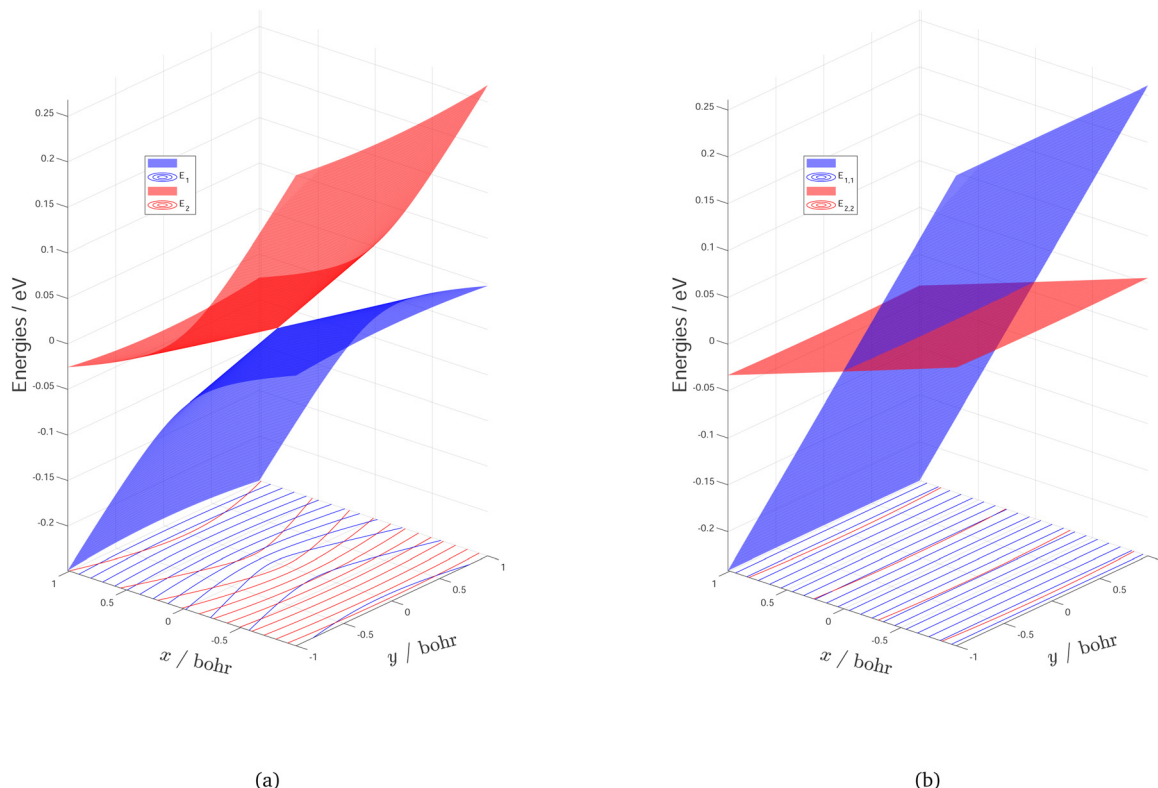


Fig. 7 Potential energy surfaces of the two lowest-lying states $1^2A'$ and $2^2A'$ of NaH_2 in adiabatic (a) and diabatic (b) representation around the lowest minimum energy crossing point (MEX) in the $g-h$ plane. The x and y indicate the magnitudes of the potential gradient difference vector \vec{g} and the interstate coupling vector \vec{h} , respectively. Zero of energy in eV is at the MEX.

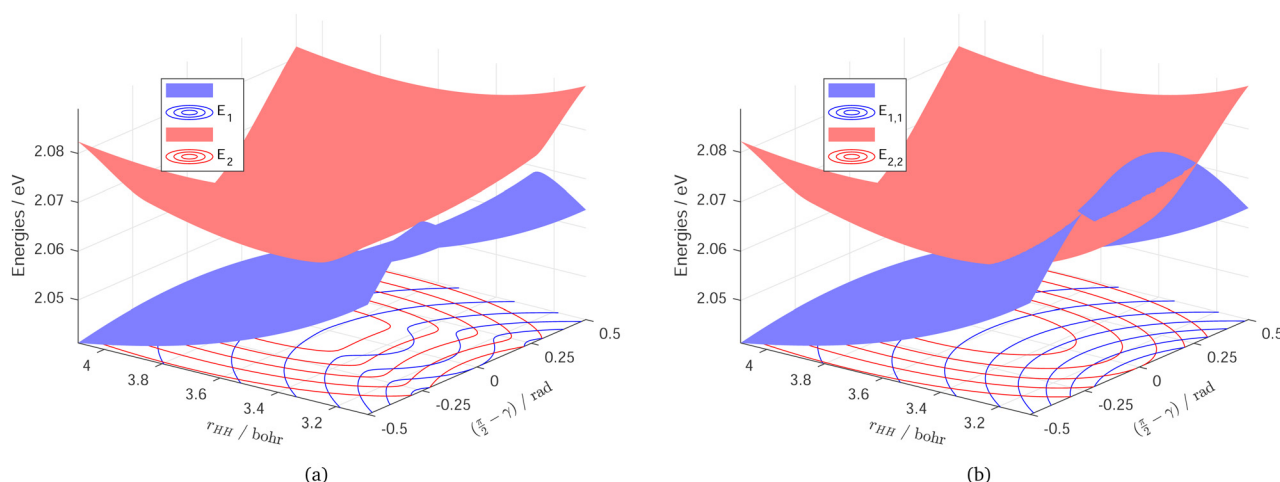


Fig. 8 Potential energy surfaces of the two lowest-lying states $1^2A'$ and $2^2A'$ of NaH_2 in adiabatic (a: E_1 and E_2) and diabatic (b: $E_{1,1}$ and $E_{2,2}$) representation in the Jacobi coordinates. r_{HH} is the H_2 bond distance, distance of Na from the center of HH mass R_{CM} is fixed at 3.0 bohr, and γ is the angle between R_{CM} and r_{HH} . Zero of energy in eV is at Na infinitely far from H_2 on the ground surface.

quantum dynamic calculations serve as a powerful tool for exploring and comparing the features of potential energy surfaces.^{50,55} To demonstrate the qualities of the diabatization and NN fitting, we conducted quantum dynamic calculations that provided accurate results on the surfaces. These calculations are performed on both the benchmark and our DPEMs,

respectively. The numerical parameters for the quantum time-dependent wave packet calculations^{56,57} are shown in Table 3. The initial wave packet was placed on the excited electronic state with H_2 in its ground ro-vibrational state.

In the vicinity of a CI, electronic states strongly interact with each other through derivative-couplings, which the BO

Table 3 Numerical parameters used in the quantum reactive scattering wave packet calculations (atomic units are used, unless otherwise stated)

Grid range and size	$R \in [0.8, 13.6]$	$N_R = 256$
Rotational basis size	$r \in [0.8, 13.6]$	$N_r = 256$
	$j_{\min} = 0$	$N_j = 64$
Initial wave packet	$J_{\max} = 130$	
	$E_0 = 1.0$ eV	$R_0 = 13.0$
	$\Delta R = 0.01$	
Dividing plane	$r = 3.0$	
Total propagation	10 000.0 iterations	
Time step	20.0 attoseconds	
Energy step	0.0001	
Highest J	100	

approximation neglects.^{58,59} It has been pointed out that conducting dynamic studies in the adiabatic representation without considering the geometric phase (GP) factor may yield qualitatively inaccurate outcomes.^{59–61} In Fig. 9, the wave functions of the two lowest-lying states obtained in the g – h plane are compared in the diabatic and adiabatic representations, respectively, in the quantum mechanical framework. The time-dependent wave packet calculations on HT and our DPEMs reveal a node on the right side ($x > 0$) in Fig. 9(a) and (c), respectively, demonstrating that the non-adiabatic interactions around the CI region interfere. The GP makes parts of a nuclear wave packet traveling on different sides from the CI point to acquire the opposite phases. In the adiabatic representation, on the other hand, such a node is absent in Fig. 9(b) and (d) due to the fact that the geometry-dependent phase factor is missing. These conclusions are consistent with the recent work of Izmaylov and co-workers,^{62–64} which explored the GP effects on nuclear dynamics of the isolated

subsystem. It should be noted that there is a slight disparity in the magnitude of the wave functions obtained from HT and our DPEMs. This difference may be due to the fact that the fitted relative values of derivative-coupling for geometries near the MEX on our DPEM are not as large as those on the HT DPEM.

In Fig. 10, the reaction probabilities for the $\text{Na}(3p) + \text{H}_2 (\nu = 0, j = 0) \rightarrow \text{NaH} (\nu \leq 5, j \leq 100) + \text{H}$ reaction are calculated using the time-dependent wave packet approach. The initial wave packet is placed on the excited electronic state with H_2 in its ground ro-vibrational state to simulate the electronically nonadiabatic reaction involving CI. Despite the very slight difference for population ratio (B_2/A_1), the original DPEM and our newly constructed one yield almost identical product population ratios over a wide energy range, which validates our new diabatization method and NN fitting procedures.

4 Summary and conclusions

In this work, a new scheme for the construction of a quasi-diabatic representation is proposed. By integrating $\nabla(E_{1,1}^d - E_{2,2}^d)$, this method is capable of performing high-precision ADT transformations, with a unique advantage in effectively handling the significant fluctuations in derivative-couplings caused by CI seams. The above scheme is applied to the DPEM construction of the $\text{Na}(3p) + \text{H}_2 \rightarrow \text{NaH} + \text{H}$ reaction, including the exciplex and the MEX properly. The produced DPEM can effectively describe nonadiabatic processes involving different electronic states. Quantum dynamical calculations were performed on the new DPEM and the previous benchmark DPEM, and the obtained results demonstrate the effectiveness of our scheme.

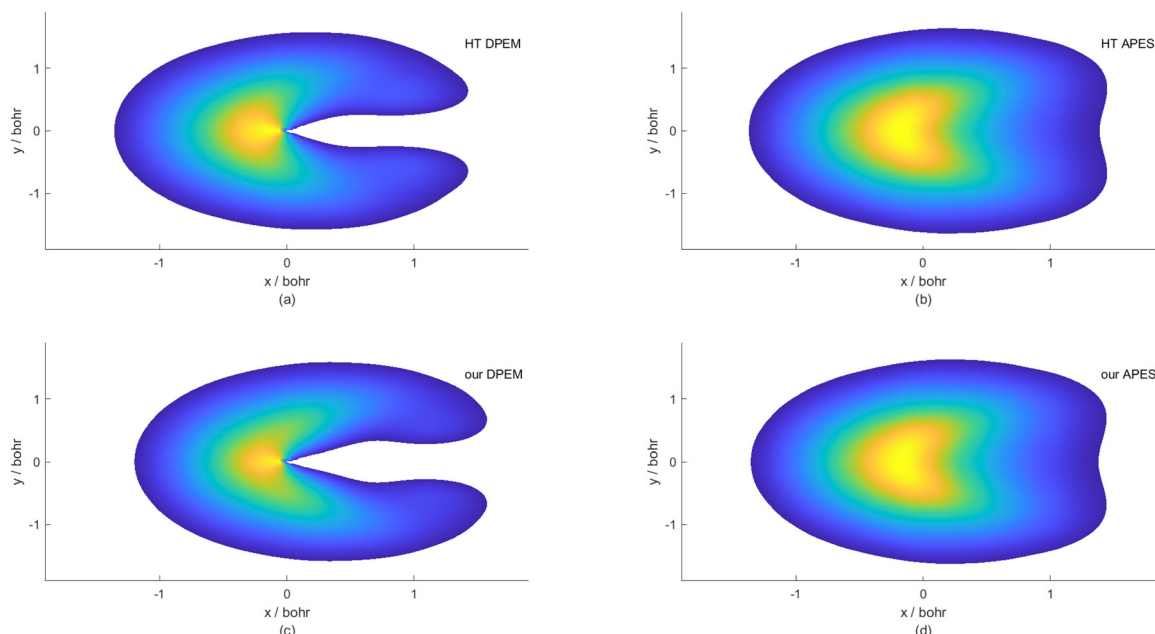


Fig. 9 Modulus of the wave functions for the two lowest-lying states in the g – h plane with the movement of wave packets from left to right on the diabatic/adiabatic PESs. Time-dependent wave packet calculations are carried out on the HT DPEM (a), HT APES (b), our new DPEM (c) and APES (d), respectively. The total propagation time is 450.0 attoseconds and R_0 for the initial wave packet is 13.0 bohr. The x and y indicate the magnitudes of the potential gradient difference vector \vec{g} and the interstate coupling vector \vec{h} , respectively.

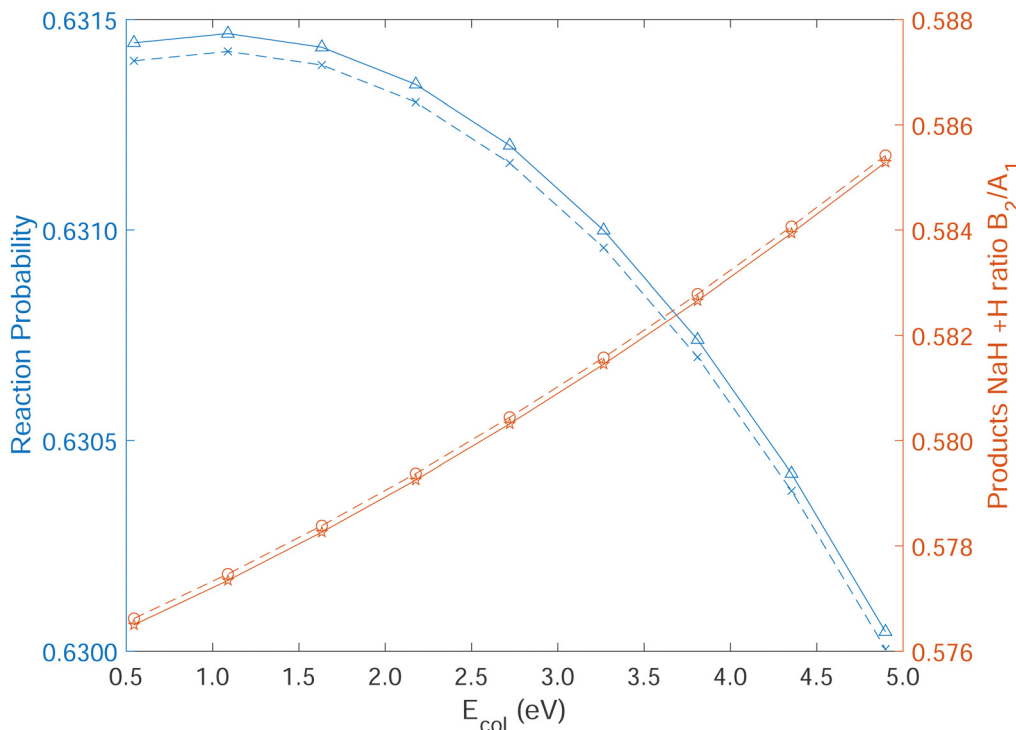


Fig. 10 Reaction probability (HT: blue triangle, ours: blue cross) and product population ratio (B_2/A_1 , HT: red cycle, ours: red star) for the $\text{Na}(3p) + \text{H}_2 (\nu = 0, j = 0) \rightarrow \text{NaH}(B_2, A_1, \nu \leq 5, j \leq 100) + \text{H}$ reaction as a function of the initial collisional energy (in eV) in the quantum time-dependent wave packet calculations on our DPEM and HT DPEM. The total propagation time is 10 000.0 attoseconds and R_0 for the initial wave packet is 13.0 bohr.

This approach is expected to be extended to larger molecular systems, and would be helpful for dynamics simulations of nonadiabatic processes.

Conflicts of interest

There are no conflicts to declare.

Acknowledgements

This work is supported by the National Natural Science Foundation of China (no. 22133003, 22320102004) and the Beijing Municipal Natural Science Foundation (no. 8212043). We thank Professor David R. Yarkony for the valuable discussions on the derivative-coupling based fitting procedure. We thank Professor Burkhard Schmidt and Professor Ulf Lorenz for providing the codes for time-dependent wave packets and many discussions on the QD calculations.

References

- 1 C. Petrongolo, G. Hirsch and R. J. Buenker, *Mol. Phys.*, 1990, **70**, 825–834.
- 2 C. R. Evenhuis and M. A. Collins, *J. Chem. Phys.*, 2004, **121**, 2515–2527.
- 3 S. Nangia and D. G. Truhlar, *J. Chem. Phys.*, 2006, **124**, 124309.
- 4 Y. Guan, D. H. Zhang, H. Guo and D. R. Yarkony, *Phys. Chem. Chem. Phys.*, 2019, **21**, 14205–14213.
- 5 Y. Shu and D. G. Truhlar, *J. Chem. Theory Comput.*, 2020, **16**, 6456–6464.
- 6 C. L. Malbon, B. Zhao, H. Guo and D. R. Yarkony, *Phys. Chem. Chem. Phys.*, 2020, **22**, 13516–13527.
- 7 Y. Shen and D. R. Yarkony, *J. Phys. Chem. A*, 2020, **124**, 4539–4548.
- 8 Y. Liu, H. Song, D. Xie, J. Li and H. Guo, *J. Am. Chem. Soc.*, 2020, **142**, 3331–3335.
- 9 Y. Liu and J. Li, *J. Phys. Chem. Lett.*, 2022, **13**, 4729–4738.
- 10 P. Botschwina, W. Meyer, I. V. Hertel and W. Reiland, *J. Chem. Phys.*, 1981, **75**, 5438–5448.
- 11 H. Werner and W. Meyer, *J. Chem. Phys.*, 1981, **74**, 5802–5807.
- 12 L. S. Cederbaum, J. Schirmer and H. D. Meyer, *J. Phys. A: Math. Gen.*, 1989, **22**, 2427.
- 13 A. J. Dobbyn and P. J. Knowles, *Mol. Phys.*, 1997, **91**, 1107–1124.
- 14 W. Domcke, D. R. Yarkony and H. Koppel, *Conical Intersections*, World Scientific, 2004.
- 15 H. Köppel, W. Domcke and L. S. Cederbaum, *Multimode Molecular Dynamics Beyond the Born-Oppenheimer Approximation*, John Wiley Sons, Ltd, 2007, pp. 59–246.
- 16 M. Boggio-Pasqua, A. I. Voronin, P. Halvick, J.-C. Rayez and A. J. C. Varandas, *Mol. Phys.*, 2010, **98**, 1925–1938.
- 17 V. C. Mota, P. J. S. B. Caridade and A. J. C. Varandas, *Int. J. Quantum Chem.*, 2011, **111**, 3776–3785.

18 D. Opalka and W. Domcke, *J. Chem. Phys.*, 2013, **138**, 224103.

19 D. M. G. Williams and W. Eisfeld, *J. Chem. Phys.*, 2018, **149**, 204106.

20 F. G. D. Xavier and A. J. C. Varandas, *Mol. Phys.*, 2021, **119**, e1904157.

21 Y. Guan, D. R. Yarkony and D. H. Zhang, *J. Chem. Phys.*, 2022, **157**, 014110.

22 Y. Shu, Z. Varga, S. Kanchanakungwankul, L. Zhang and D. G. Truhlar, *J. Phys. Chem. A*, 2022, **126**, 992–1018.

23 J. Chen, H. Zhang, L. Zhou, X. Hu and D. Xie, *Phys. Chem. Chem. Phys.*, 2023, **25**, 26032–26042.

24 J. Wang, F. An, J. Chen, X. Hu, H. Guo and D. Xie, *J. Chem. Theory Comput.*, 2023, **19**, 2929–2938.

25 Y. Hong, Z. Yin, Y. Guan, Z. Zhang, B. Fu and D. H. Zhang, *J. Phys. Chem. Lett.*, 2020, **11**, 7552–7558.

26 X. Zhu, *Dissertation: The Quasi-Diabatic Hamiltonian Approach to Accurate and Efficient Nonadiabatic Dynamics with Correct Treatment of Conical Intersection Seams*, Johns Hopkins University, Baltimore, Maryland, 2014.

27 D. R. Yarkony, *J. Chem. Phys.*, 1996, **104**, 2932–2939.

28 D. Yarkony, *Rev. Mod. Phys.*, 1996, **68**, 985–1013.

29 D. R. Yarkony, *J. Chem. Phys.*, 2004, **121**, 628–631.

30 M. S. Schuurman and D. R. Yarkony, *J. Chem. Phys.*, 2007, **127**, 094104.

31 X. Zhu and D. R. Yarkony, *J. Chem. Phys.*, 2012, **136**, 174110.

32 X. Zhu and D. R. Yarkony, *J. Phys. Chem. A*, 2015, **119**, 12383–12391.

33 Y. Wang and D. R. Yarkony, *J. Chem. Phys.*, 2018, **149**, 154108.

34 M. Baer, *Beyond Born–Oppenheimer: Conical Intersections and Electronic Nonadiabatic Coupling Terms*, John Wiley & Sons, Inc., 2006.

35 M. A. Collins, O. Godsi, S. Liu and D. H. Zhang, *J. Chem. Phys.*, 2011, **135**, 234307.

36 Z. Yin, B. J. Braams, Y. Guan, B. Fu and D. H. Zhang, *Phys. Chem. Chem. Phys.*, 2021, **23**, 1082–1091.

37 I. V. Hertel, *Collisional Energy-Transfer Spectroscopy with Laser-Excited Atoms in Crossed Atom Beams: A New Method for Investigating the Quenching of Electronically Excited Atoms by Molecules*, John Wiley and Sons, Ltd, 1981, pp. 341–398.

38 D. R. Yarkony, *J. Chem. Phys.*, 1986, **84**, 3206–3211.

39 M. D. Hack and D. G. Truhlar, *J. Chem. Phys.*, 1999, **110**, 4315–4337.

40 D. W. Schwenke, S. L. Mielke, G. J. Tawa, R. S. Friedman, P. Halvick and D. G. Truhlar, *Chem. Phys. Lett.*, 1993, **203**, 565–572.

41 W. T. Zemke, R. E. Olson, K. K. Verma, W. C. Stwalley and B. Liu, *J. Chem. Phys.*, 1984, **80**, 356–364.

42 J. A. Silver, N. C. Blais and G. H. Kwei, *J. Chem. Phys.*, 1979, **71**, 3412–3427.

43 E. Gislason, A. Kleyn and J. Los, *Chem. Phys.*, 1981, **59**, 91–109.

44 A. Thiel and H. Koppel, *J. Chem. Phys.*, 1999, **110**, 9371–9383.

45 D. R. Yarkony, *J. Chem. Phys.*, 1996, **105**, 10456–10461.

46 C. L. Malbon, X. Zhu, H. Guo and D. R. Yarkony, *J. Chem. Phys.*, 2016, **145**, 234111.

47 C. L. Malbon and D. R. Yarkony, *J. Chem. Phys.*, 2017, **146**, 134302.

48 Y. Wang, Y. Guan and D. R. Yarkony, *J. Phys. Chem. A*, 2019, **123**, 9874–9880.

49 Y. Guan and D. R. Yarkony, *J. Phys. Chem. Lett.*, 2020, **11**, 1848–1858.

50 F. Li, X. Yang, X. Liu, J. Cao and W. Bian, *ACS Omega*, 2023, **8**, 17296–17303.

51 F. Li, X. Liu, X. Yang, J. Cao and W. Bian, *Chin. J. Chem. Phys.*, 2023, **36**, 545–552.

52 H. Longuet-Higgins, *Mol. Phys.*, 1963, **6**, 445–460.

53 O. Godsi, C. R. Evenhuis and M. A. Collins, *J. Chem. Phys.*, 2006, **125**, 104105.

54 S. Wang, Z. Yang, J. Yuan and M. Chen, *Sci. Rep.*, 2018, **8**, 17960.

55 J. Luo, J. Cao, H. Liu and W. Bian, *Chin. J. Chem. Phys.*, 2022, **35**, 185–192.

56 B. Schmidt and U. Lorenz, *Comput. Phys. Commun.*, 2017, **213**, 223–234.

57 B. Schmidt and C. Hartmann, *Comput. Phys. Commun.*, 2018, **228**, 229–244.

58 X. Liu, W. Bian, X. Zhao and X. Tao, *J. Chem. Phys.*, 2006, **125**, 074306.

59 Y. Wu, C. Zhang and H. Ma, *RSC Adv.*, 2017, **7**, 12074–12084.

60 H. von Busch, V. Dev, H.-A. Eckel, S. Kasahara, J. Wang, W. Demtroder, P. Sebald and W. Meyer, *Phys. Rev. Lett.*, 1998, **81**, 4584–4587.

61 M. Keil, H.-G. Kramer, A. Kudell, M. Baig, J. Zhu, W. Demtroder and W. Meyer, *J. Chem. Phys.*, 2000, **113**, 7414–7431.

62 I. G. Ryabinkin and A. F. Izmaylov, *Phys. Rev. Lett.*, 2013, **111**, 220406.

63 L. Joubert-Doriol, I. G. Ryabinkin and A. F. Izmaylov, *J. Chem. Phys.*, 2013, **139**, 234103.

64 A. F. Izmaylov, J. Li and L. Joubert-Doriol, *J. Chem. Theory Comput.*, 2016, **12**, 5278–5283.